Experimental Assessment of Measurement Uncertainty for a Green-Wavelength LiDAR System

Yu Lan[1], Jiale Wang[1], Ji Yang[1], Mario Kolling[1], Alexander Dorndorf[1],
Christoph Werner[2], Alexander Reiterer[2, 3], Jens-André Paffenholz[1]

[1] Institute of Geotechnology and Mineral Resources – Geomatics, Clausthal University of Technology
38678 Clausthal-Zellerfeld, Germany - yu.lan@tu-clausthal.de
[2]Fraunhofer Institute for Physical Measurement Techniques IPM, 79110 Freiburg, Germany
[3]Institute for Sustainable Systems Engineering (INATECH), University Freiburg, 79110 Freiburg, Germany

Keywords: LiDAR, green-wavelength, 3D point cloud, underwater, refractive index.

Abstract:

Green-wavelength LiDAR systems enable high-resolution 3D sensing in underwater environments, but the geometric evaluation of measurements acquired across the waterline remains challenging. This is mainly because traceable reference instruments typically operate only in air, while refraction at the waterline systematically affects both the 3D point cloud and the geometry of partially submerged objects. This study presents a controlled experimental framework for assessing waterline-induced effects in an Underwater LiDAR (ULi) system, using a terrestrial laser scanner (TLS), the Z+F IMAGER 5016A (IMAGER), as an above-water reference. A rigid reference frame (RRF) spanning the waterline was deployed in a swimming pool. First, the RRF was scanned by the IMAGER under in-air conditions to establish its reference geometry. Subsequently, in the waterline configuration, the ULi system measured the complete RRF, while the IMAGER captured only its above-water part. The analysis investigated refraction- and interface-related effects on the 3D point cloud and geometry in the above-water, cross-waterline, and underwater parts of the RRF. For a physically meaningful assessment, the evaluation considered overall geometric deviations and rigid-body-invariant internal quantities, including pairwise distances, which are independent of the overall pose of the RRF. Refractive-index sensitivity was analyzed by perturbing the refractive index and quantifying the resulting changes in the derived geometric quantities. The proposed workflow provides a practical and traceable basis for isolating waterline-related refraction effects, evaluating their impact on 3D point cloud geometry, and assessing refractive-index sensitivity.

1. Introduction and motivation

Green-wavelength LiDAR has emerged as a practical solution for accurately mapping underwater structures. An underwater LiDAR (ULi) system developed by the Fraunhofer Institute for Physical Measurement Techniques (IPM), is purpose-built for high-resolution underwater inspection and mapping (Werner et al., 2023; Fraunhofer IPM, 2025). Conventional near-infrared (NIR) (terrestrial) laser scanners fail to observe submerged structures because water strongly absorbs NIR radiation. Existing studies on the ULi system have investigated its performance in air and water. By analyzing both random error and systematic bias, Lan et al. (2026) demonstrated that the ULi system can achieve millimeter-level measurement accuracy in air medium. In the short-range distances of 2 m to 5 m one can reach a precision at about 1 mm level. This confirms the high geometric quality of the ULi system in the air condition environment and provides an important reference for subsequent analyses of water-related measurement effects.

Under underwater conditions, previous studies mainly evaluated the resolution capability of the ULi system. According to Walter et al. (2025), the ULi system was systematically tested in two laboratory scenarios and one real-world scenario to assess its suitability for high-resolution monitoring of underwater infrastructure. In a close-range static tank experiment under clear water conditions with Nephelometric Turbidity Units (NTU) to be 0, the ULi system was able to detect man-made and organic structures down to 2.36 mm at a close range ($\leq$ 0.56 m), demonstrating millimeter-scale level of detail. A second static laboratory experiment from 1.03 m to 8.03 m, using a Boehler star target, showed that arc segments of 2.95 mm could be fully resolved at distances up to 8.03 m. In contrast, the field trial in the river Elbe generated no meaningful reflections from infrastructure targets, and the authors attributed this result to the comparatively high turbidity of the water under the surveyed field conditions (6 NTU; Secchi depth 1.10 m).

Heffner et al. (2025) performed static scans of a Boehler star, spheres and metal plates at different ranges and under varying turbidity levels. Repeated measurements on a metal plate were used to derive precision and accuracy metrics. In addition, they reported a range precision of 1.95 mm and a mean relative range accuracy of 6.01 mm. Furthermore, they demonstrated that small objects such as shells and water plants can still be clearly identified in low- to moderate-turbidity conditions.

Heffner et al. (2026) investigated the suitability of the ULi system for high-resolution underwater monitoring under varying temperature and salinity conditions, with a view towards combined monitoring with distributed fiber optic sensing (DFOS). They showed that the ULi system achieves temperature-independent sub-millimeter 3D point cloud precision of about $\pm$0.6 mm and can detect deformations smaller than 1 cm with a mean accuracy of about 0.7 mm. At the same time, they reported a systematic temperature-related depth bias of up to 7 mm in colder water, which cannot be fully explained by refractive index correction alone and therefore requires further investigation. Overall, the authors highlight the strong potential of the ULi system for precise underwater surface monitoring, while also stressing the need to better understand temperature-dependent systematic effects before multi-epoch comparisons under different water conditions.

In applications with partially flooded adits, there is a need for underwater and in-air data acquisition to entirely capture the structure’s geometry. To address this mixed-medium scenario, an efficient approach is to solely use the ULi system for data acquisition. This results directly in a single and unique coordinate frame for both media by positioning the ULi system at the waterline so that it simultaneously acquires the structures under and above the waterline. This paper focuses on evaluating the influence of waterline conditions on the 3D point cloud and geometric performance of the ULi system, whereas the Zoller+Fröhlich (Z+F) IMAGER 5016A (IMAGER) is used as reference sensor.

This present work addresses the following questions:

- What geometric distortions occur when both the above-water and underwater parts of the 3D point cloud are reconstructed using the same refractive-index configuration?
- How sensitive are the reconstructed geometries to the selected refractive index?
- How accurately can the ULi system reconstruct geometry at the waterline?
- How do refraction and interface-related effects affect the 3D reconstruction of partially submerged objects?

2. Methodology and experimental setup

2.1 ULi system

3D point cloud spacing is used as a geometric indicator of the LiDAR system’s spatial resolution and point density. The ULi system employs two primary scanning patterns: circle shaped and line shaped. This paper focuses on the circle pattern. In this paper, the ULi system shown in Figure 1 in its waterline setup is operated with the configuration shown in Table 1. Since the water quality in the swimming pool was excellent during the experiment (NTU = 0), the filter type/power mode of the ULi system is set to be adjustment, which means the green laser is emitted with a strength at the lowest possible laser class 2M (Walter et al., 2025). A motor speed of 25 Hz means that the rotating prism completed 25 revolutions per second. The cycle time was set to be 20 s, where one scan cycle consisted of one outward spiral and one inward spiral. The initial radius was therefore kept at 0 m. The range gating was set to 0 to 15 m to ensure that the targets and other relevant objects within the swimming pool scene were captured as completely as possible. The pulse repetition rate was set to 100,000 Hz.

Configuration	Value
Power mode	Adjustment
Cycle time (s)	20
Radius (Initial radius) (m)	0
Range gating (m)	0 to 15
Pulse repetition rate	100,000 Hz
Motor speed (Hz)	25

Table 1 Scan configuration of the ULi system

With this configuration, all targets/objects within the swimming pool were scanned by the ULi system. If only a single cycle from the ULi system is used, its 3D point cloud becomes too sparse, which would adversely affect the subsequent 3D point cloud processing. Therefore, at each measurement distance, the 3D point clouds from several cycles were merged and processed jointly. In addition, based on the data analyzed in this study and according to Lan et al. (2026), the ULi system exhibits a millimeter-level drift over time due to internal hardware-related effects. At present, this drift appears to remain within an acceptable range.

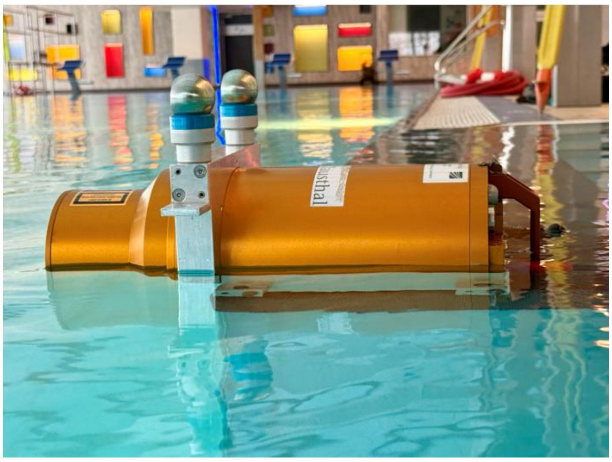

Figure 1 ULi system at the waterline.

2.2 Experimental setup

This study is based on a controlled experiment conducted in a swimming pool to evaluate the performance of the ULi system under waterline measurement conditions. Figure 2 shows the experimental setup. The rigid reference frame (RRF) was firmly fixed in a water depth of about 1 m. The swimming pool floor has a certain slope. The total station and the IMAGER were used to establish and monitor the RRF geometry above water. The ULi system was positioned at the waterline, refer to Figure 2 for an overview and Figure 1 for the details with respect to the waterline positioning.

The ULi system was evaluated in a controlled dual-scanner experiment using the RRF with fixed and known geometry given by in total 13 targets (Figure 3). As targets are used classical 4-fold black and white targets (b/w targets) of two different sizes (200 mm × 200 mm, 150 mm × 150 mm) as well as spherical targets (sphere) with a radius of 100 mm. Refer to Figure 3 and Table 2 for dimensions, spatial distribution as well as labeling of the targets on the RRF.

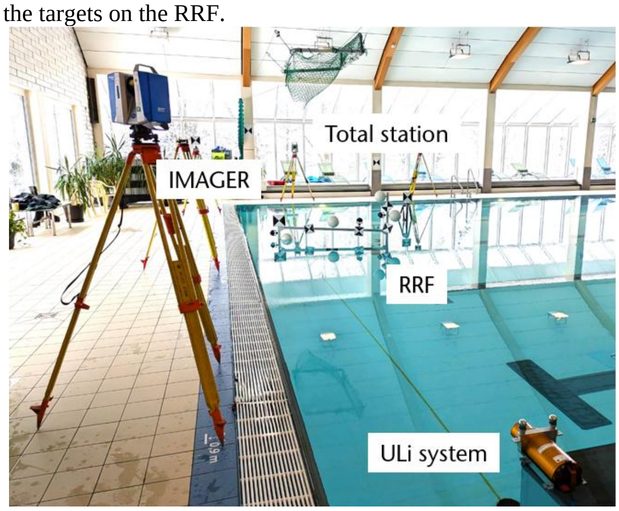

Figure 2 Overview of the experimental setup of the ULi system (bottom right), and the RRF in the swimming pool as well as on the swimming poolside the IMAGER (left side) and the total station (background).

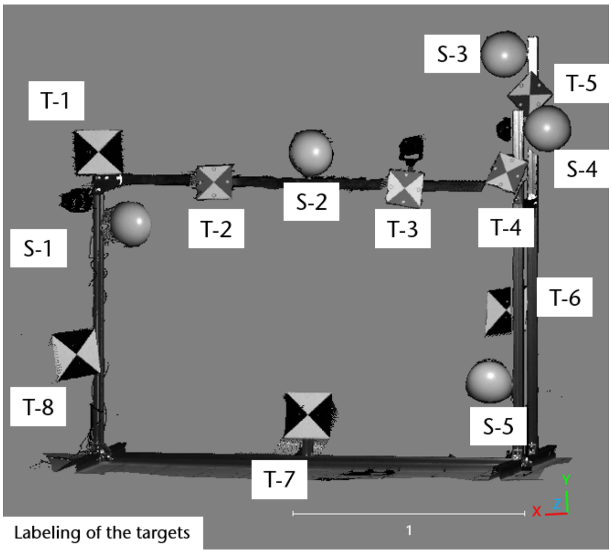

Figure 3 Definition of the b/w targets and spheres on the RRF.

Item	Dimension	Labels
b/w targets	150 mm × 150 mm	T-2, T-3, T-4, T-5
b/w targets	200 mm × 200 mm	T-1, T-6, T-7, T-8
Sphere	Radius: 100 mm	S-1 to S-5

Table 2 b/w targets and spheres in the experiment.

The RRF carries in total eight uniformly distributed above-water targets which are five b/w targets and three spheres. One sphere is located at the waterline, and three b/w targets together with one sphere are mounted underwater (See Figure 3). The RRF is assumed to behave as a rigid object, so that deviations observed under waterline conditions can be attributed primarily to refraction and air-water interface effects rather than to structural deformation. Before placing the RRF in the swimming pool, 3D point clouds of the geometry of the RRF are captured as an in-air baseline by means of the IMAGER. In subsequent 3D point cloud processing steps, pairwise target distances are calculated as reference quantities such as b/w target to b/w target, b/w target to sphere, and sphere to sphere distances. The RRF is then placed in the swimming pool and repeatedly scanned by the ULi system at stand-off distances of approximately 5 m, 6 m, and 7 m. ULi measurements acquired under waterline conditions are evaluated based on the IMAGER-defined in-air reference using pairwise target distances. The analysis includes representative pairwise target distances in order to quantify the influence of refraction and air-water interface effects on the reconstructed 3D geometry. In addition, the sensitivity of these geometric quantities to the refractive index setting is assessed by changing the refractive index used in the processing.

2.3 Analysis strategy to maintain a cross-medium reference

For each range measurement, the raw data are initially processed using a medium-specific parameter file, such as an air configuration or a water configuration. However, when the entire raw dataset is processed with the configuration of only one medium, the dimensions of the points belonging to the other medium become distorted. Therefore, the raw dataset was processed with two different medium-specific configuration files, the resulting 3D point clouds must be segmented at the water-air interface and then merged. In this way, the 3D points corresponding to each medium retain the correct dimensions.

To assess the 3D geometry of the RRF captured by the ULi system in the waterline, the IMAGER-derived 3D point cloud of the RRF acquired at swimming poolside was used as reference. For this purpose, both 3D point clouds must first be transformed into a common coordinate system. Because the IMAGER cannot capture the submerged part of the RRF, the above-water targets, which are observed by both the IMAGER and the ULi system in the pool experiment, are used as common reference features for registration. In this way, the swimming poolside IMAGER-based RRF can be transformed into the pool measurement configuration, and the ULi system-based 3D point cloud can be aligned with the IMAGER-based reference for the subsequent evaluation. The centers of the b/w targets are estimated according to the method of Janßen et al. (2019). Subsequently, the Helmert 3D transformation is applied to estimate a rigid transformation $(\boldsymbol{R}, \boldsymbol{t})$ between IMAGER and ULi system and the scale is set to be 1 (Paffenholz & Bae, 2012).

$$\boldsymbol{x}_{ULi,k} = \boldsymbol{R}\boldsymbol{x}_{IMAGER,k} + \boldsymbol{t} \tag{1}$$

In Equation 1, let $k = 1$ to K, where K indexes the corresponding target centers. Here, $\boldsymbol{R}$ is the rotation matrix and $\boldsymbol{t}$ is the translation vector between the sensor-defined coordinate system of the IMAGER and the ULi system, respectively. $\boldsymbol{x}_{IMAGER,k}$ is the coordinate from the IMAGER. Using the targets, the alignment quality is assessed from the residuals at these control points after applying the estimated rigid transformation.

The sphere with known radius of $r = 100$ mm is used in all scenarios (air medium, water medium and cross-medium along the waterline). For each 3D point cloud, segmented sphere points are used to estimate only the center while keeping r fixed to its known value. The same geometric model is used in all media, but adapt the estimator for robustness under partial coverage. Following Zhou et al. (2008), sphere centers were estimated based on:

$$min = \sum_h \left(\sqrt{(x_h - x_0)^2 + (y_h - y_0)^2 + (z_h - z_0)^2} - r \right)^2 \tag{2}$$

Where x_h, y_h and z_h denote the coordinates of a point in the 3D point cloud on the sphere surface, x_0, y_0 and z_0 denote the coordinates of the sphere center.

2.4 Refractive index of different media and wavelength

Since the ULi system is a time-of-flight (TOF) LiDAR operating at a wavelength of λ=532 nm, the propagation of the laser pulse in water should be described using the group refractive index rather than the (phase) refractive index.

Schwarz et al. (2020) showed that, for pulsed hydrographic laser measurements, the group refractive index $n_{water,g}$ is the relevant quantity for time-to-range conversion and can be derived from the wavelength-dependent refractive index according to Zhang et al. (2019), the group refractive index can be estimated by Equation 3:

$$n_{water,g} = n_{water} - \lambda \cdot \frac{dn_{water}}{d\lambda} \tag{3}$$

Where n_{water} is the refractive index in the water.
For the present swimming pool experiment, the refractive index n_{water} was estimated using the empirical formulation of Höhle (1971).

$$n_{water} = 1.338 + 4 \cdot 10^{-5} \cdot (486 - \lambda - T + 0.003 \cdot D + 5 \cdot S) \tag{4}$$

Where T is the water temperature in ℃, D is the propagation distance in water in m, and S is the salinity in ‰. In the present study, the swimming pool water was considered near-freshwater, because the chlorine concentration used for disinfection (0.35 mg/L) is negligible compared with salinity levels at which seawater effects become relevant. Accordingly, the salinity term was set to $S=0$. Temperature effects were explicitly considered, and the parameter T was assigned according to the measured swimming pool water temperature during the experiment.

3. Results and discussion

3.1 The reference structure above water – creating the reference by IMAGER

The scanning resolution of the IMAGER is set to be “superhigh” and the spacing of it is about 3.1 mm @10 m (Zoller + Fröhlich GmbH, 2026). Additionally, the 3D point cloud from IMAGER exhibits a regular, raster-like distribution.

Prior to putting the RRF in the swimming pool, two 3D point clouds were acquired. The centers of the b/w targets and spheres were extracted from both 3D point clouds, and the corresponding inter-center distances were compared. The average difference in the derived center distances between the two 3D point clouds is 0.05 mm, demonstrating high stability and repeatability of the center estimation. Therefore, the RRF obtained from the IMAGER 3D point cloud was adopted as the ground truth for the subsequent evaluation. Due to its unfavorable observation geometry, T-6 target was excluded from the subsequent evaluation, as its inclusion would bias the subsequent assessment. In addition, after the RRF was removed from the swimming pool, a 3D point cloud was acquired with the IMAGER as a stability check to confirm that no significant deformation or displacement had occurred during transfer in and out of the swimming pool. Comparison of the averaged internal pairwise b/w target and sphere center distances derived from the 3D point clouds before putting to swimming pool and after the RRF was removed from the swimming pool (See Figure 4).

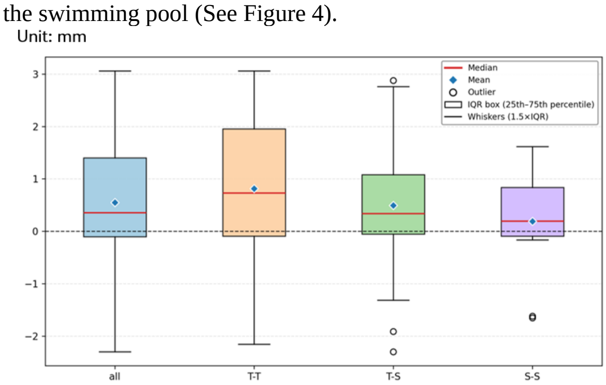

Figure 4 3D displacements of mutual targets between IMAGER in-air 3D point clouds of the RRF before and after transferring it to the swimming pool. Displacements per target type: purple colored mutual sphere (S-S), green colored b/w target to sphere (T-S), orange colored mutual b/w target and blue all target types.

Figure 4 compares the differences in the pairwise distances of the RRF between the initial measurement and the final IMAGER measurement after completing the entire data acquisition in the swimming pool. Here, all denotes all b/w target to b/w target (T-T), b/w target to sphere (T-S), and sphere to sphere (S-S) distances. Overall, the distributions are centered close to 0 mm, and the median values of all groups remain below 0.7 mm, indicating that the internal geometry of the RRF was largely preserved throughout the entire experiment and that no pronounced global deformation or displacement occurred. The mean values are slightly higher than the medians in most groups, particularly for T-T and T-S, which points to a slight positive skew caused by a small number of larger positive deviations. In addition, the T-T and T-S group exhibit slightly broader distributions than the S-S group, indicating a slightly higher dispersion for b/w target-involving pairs, while the S-S group shows the smallest dispersion. Although a few isolated outliers are visible outside the whisker range, the overall pattern supports the assumption that the RRF maintained a stable internal geometry before and after the experiment in the swimming pool, so that the initially acquired 3D point cloud of the RRF with IMAGER can be considered reliable for the subsequent evaluation.

A rigid registration was performed between the IMAGER-derived RRF 3D point cloud acquired under swimming poolside conditions and the above-water subset of the corresponding IMAGER-derived RRF point cloud acquired in the swimming pool setup. The registration was based on the three b/w targets (T-1, T-3, and T-5, see Figure 3) located above water. The resulting transformation parameters were then applied to transform the swimming poolside-RRF to the coordinate system of the swimming pool measurement configuration. Table 3 summarizes the resulting mean 3D point-to-point residuals between corresponding points after the transformation. All residuals are below 0.5 mm, confirming a very good registration quality and a stable transformation between the swimming poolside and swimming pool measurement configurations.

Distance (m)	Residual (mm)
5	0.31
6	0.41
7	0.23

Table 3 Mean 3D coordinate residuals of the three above-water targets

Another rigid registration was performed between the ULi-derived 3D point cloud of the RRF and the above-water part of the corresponding IMAGER-derived RRF 3D point cloud in the swimming pool setup. For the ULi system’s distance to the RRF ranging from 5 m, 6 m to 7 m, six to seven well distributed targets were used for each distance for the registration. These target setup consists of b/w targets mounted on the RRF, b/w targets mounted on tripods positioned around the swimming pool, and uniformly distributed b/w targets fixed on the swimming pool walls. After this registration, the ULi-derived 3D point cloud was transformed into the coordinate system of the IMAGER-derived reference point cloud in the swimming pool setup. This step enabled a consistent evaluation of both the underwater and above-water parts of the ULi measurements with respect to the complete RRF geometry represented by the IMAGER 3D point cloud. Table 4 shows the resulting mean 3D point-to-point residuals between corresponding points after the transformation from ULi system to IMAGER.

Distance (m)	Residual (mm)
5	1.1
6	1.7
7	2.0

Table 4 Mean 3D coordinate residuals of the above-water targets

Table 4 indicates that the registration between 3D point clouds of the ULi system and the IMAGER is of high quality. For all three measurement configurations, the mean 3D point-to-point residuals of the corresponding above-water targets remain at the millimeter level, demonstrating a good geometric alignment after transformation. Although the residuals increase slightly from 1.1 mm at 5 m to 2.0 mm at 7 m, the overall registration accuracy can still be considered robust and reliable for the subsequent evaluation. Although the registration was performed only on the above-water part of the RRF, the RRF was applied as a highly stable rigid structure. Therefore, it was assumed that no deformation occurred in the submerged part.

3.2 Build a combined ULi system based above and underwater 3D point cloud

In addition, the raw 3D point clouds from the ULi system are processed with explicit consideration of the different medium conditions above and under the waterline. If the same refractive index is used for the entire 3D point cloud without distinguishing between the above-water and underwater part, the resulting geometry would be systematically distorted. In particular, the reconstructed dimensions of the RRF would no longer be physically consistent, since the laser beam propagates through air and water under different refractive conditions. This would lead to biased point positions and, consequently, to inaccurate estimates of distances, dimensions, and relative feature locations across the waterline.

Figure 5(a) illustrates this effect by showing that an undifferentiated processing by using n_{air}=1.0003, i.e., same air medium configuration for the entire 3D point cloud. The above-water structure remains consistent, the submerged section of the RRF is strongly distorted. This systematic bias is consistent with the use of an inappropriate refractive index for underwater observations. In other words, the air-based parameterization can describe the signal path above the water surface, but it fails to represent the altered propagation conditions in the water. Consequently, the underwater 3D point cloud does not preserve the true object geometry. This intermediate result underlines the necessity of a medium-dependent processing strategy for waterline 3D point clouds, in which the raw 3D point clouds are processed separately with air and water specific refractive indices and subsequently merged according to the position of the waterline.

Figure 5(b) shows the result after processing the raw 3D point cloud with the proper refractive index to the medium, i.e., using the refractive index n_{water}=1.335 for the 3D point cloud part under the waterline. At a first inspection, the front view in Figure 5(b) does not reveal any pronounced differences. A closer examination of the waterline area indicates that there is still a mismatch in the depth direction, which is obvious in the side view depicted in Figure 5(c). The assumption is the use of an inappropriate refractive index for the medium water, what will be further analyzed in Section 3.3.

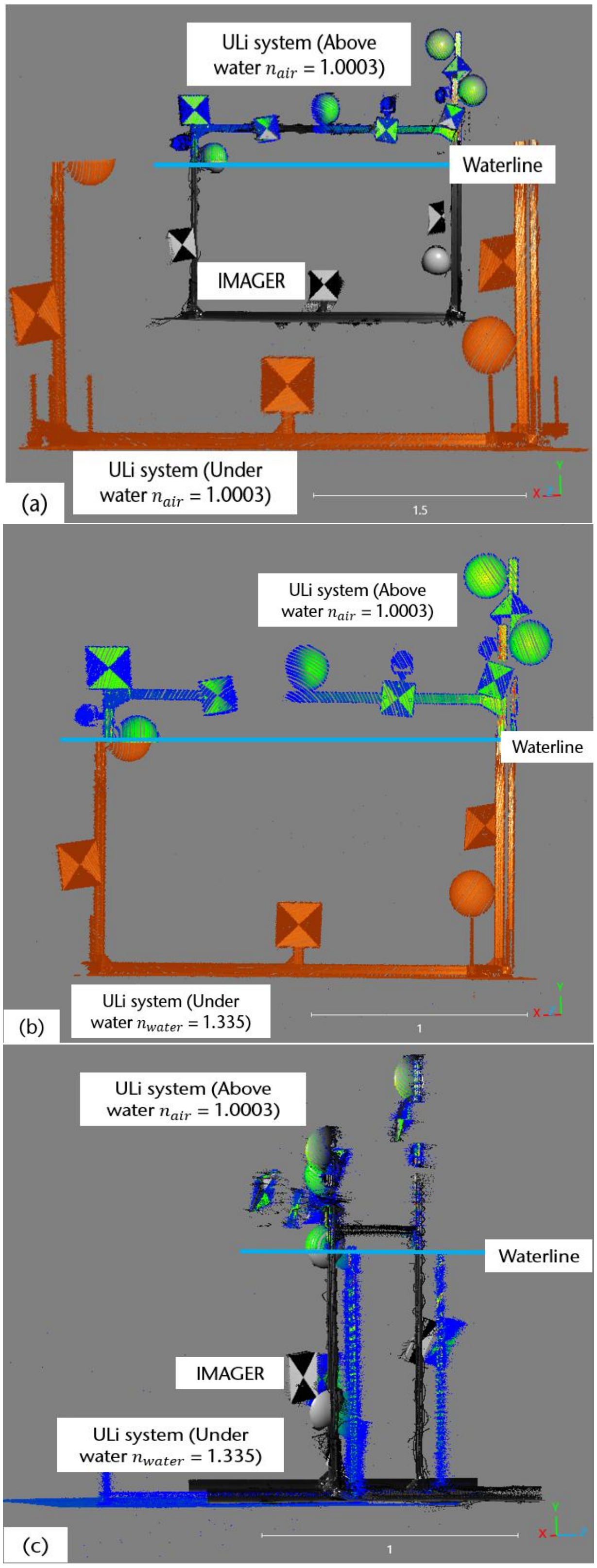

Figure 5 (a) Effect of using air processing configuration for the full 3D point cloud across the waterline; (b) Processed from the raw data using the air configuration and the water configuration, respectively, and then cropped at the waterline and merged; (c) Side view of the RRF showing significant deviations using n_{water}=1.335. Grey 3D point cloud indicates the IMAGER 3D point cloud, and the cyan line marks the waterline.

3.3 Assessment of Refractive Index Effects

Despite the applied correction strategy, a depth bias was observed in the cross-waterline region (Figure 5 (c)). According to Schwarz et al. (2020), in the case of pulsed laser propagation in water with a wavelength $\lambda = 532$ nm, the refractive index is n_{water} =1.335, while the proper group refractive index is $n_{water,g}$ =1.356. The latter is obtained from evaluating Equation 3 and Equation 4 using the laser wavelength of λ = 532 nm and a water temperature of T = 27℃.

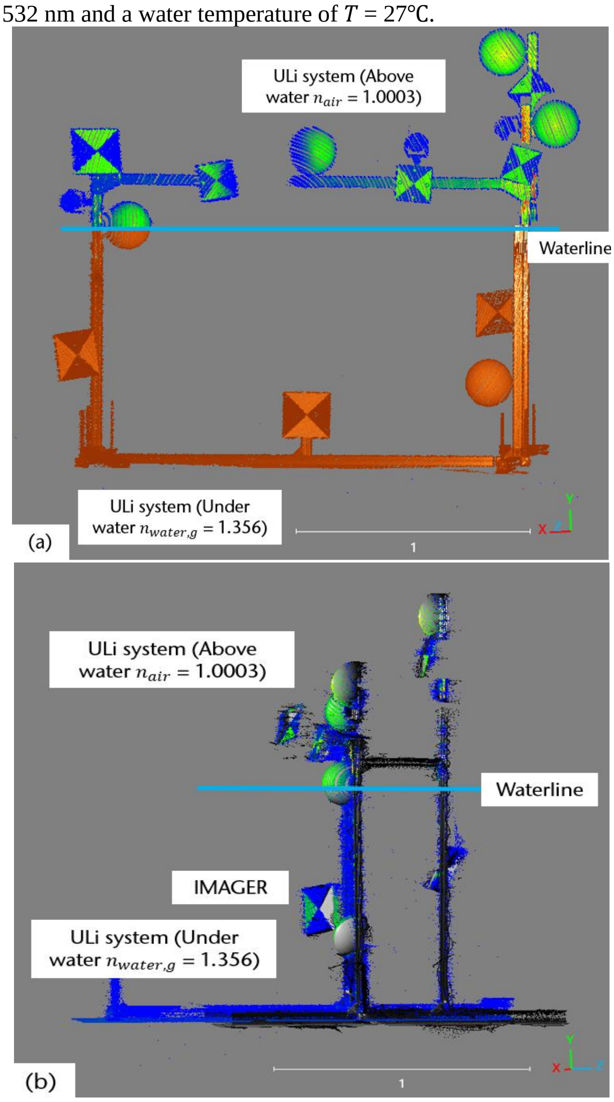

Figure 6 Comparison of 3D point cloud acquired by the ULi system and the IMAGER using the group-refractive-index settings $n_{water,g}$=1.356 for the underwater reconstruction, the IMAGER 3D point cloud is shown as the reference. (a) front view and (b) side view.

A clear correction of the measured scanning depth can be observed after applying the group refractive index. This can be clearly seen from the front view of the RRF in Figure 6(a) also for the sphere S-1 in the waterline. Moreover, Figure 6(b) shows the significantly improved correspondence in depth direction compare to the intermediate result of Figure 5(c). However, to minimize the reconstruction error, the applied group refractive index must closely match the true group refractive index.

To further analyze the influence of the group refractive index, the influence of a change of 0.001, i.e., $n_{water,g}$ =1.356 to $n_{water,g}$=1.357 is investigated and discussed in Figure 7.

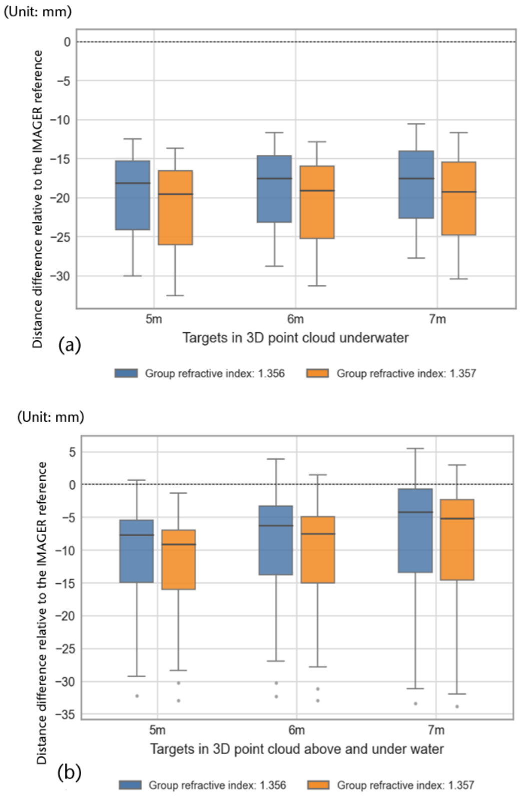

Figure 7 Distance differences relative to the mean IMAGER reference for (a) underwater and (b) cross-waterline target pairs.

Figure 7 shows a clear tendency for the underwater-affected distances, including both the fully submerged target pairs (Figure 7(a)) and the waterline-crossing target pairs (Figure 7(b)). For the fully submerged target pairs in Figure 7(a), the boxplots for $n_{water,g}$ =1.357 are consistently displaced towards more negative values compared to those for $n_{water,g}$=1.356 across the 5 m, 6 m, and 7 m datasets, with lower median values in all cases. The interquartile ranges of the two settings remain broadly comparable and still overlap, which suggests that the main effect is not a substantial increase in dispersion, but a systematic shift of the distributions towards more negative distance differences. In Figure 7(b), a similar but weaker downward shift can be observed for the waterline-crossing target pairs, where the overlap between the two distributions is more pronounced. The remaining biases are still on the centimeter level and the distributions of the two tested settings still overlap to some extent, which suggests that the change of the group refractive index worsens the overall alignment with the IMAGER reference. However, keeping $n_{water,g}$=1.356 does not fully eliminate the residual systematic deviations. These remaining errors likely reflect a combination of factors, including the fitting uncertainties of the b/w target and sphere centers as well as the fact that the applied group refractive index, although improved, is still not fully optimal for the actual measurement conditions.

To shortly resume, after replacing the refractive index with the group refractive index, the systematic bias was reduced. In particular, the RRF acquired by the ULi system showed a much better alignment with the RRF acquired by the IMAGER under swimming poolside conditions, indicating that the use of the group refractive index provides a more physically consistent description of pulse propagation for the present TOF measurements. However, whether a complete alignment can be achieved still requires further investigation. This is because the refractive index is not a fixed quantity, but depends on several environmental factors, including water, temperature, pressure, and composition. As a result, even after introducing the group refractive index, residuals may remain if the adopted group refractive index does not fully represent the actual measurement conditions.

3.4 Investigation of RRF structure in different media

To investigate the influence of refraction ($n_{water,g}$=1.356) at the waterline on the geometric relationships between above water and underwater parts of the RRF, only a representative subset of pairwise target distances were selected from the b/w targets and sphere of the structure. The selection was based on the geometric configuration of the RRF and by the objective of identifying waterline-related bias. The pairwise target distances were grouped into three categories: above-water, cross-medium, and underwater.

3.4.1 RRF structure in medium air using above-water targets: The above-water target distances using T-1, T-5, S-2 and S-4 are discussed according to Figure 8. It can be noted that the above-water targets exhibit the smallest distance differences relative to the targets stemming from the IMAGER 3D point cloud. The ULi system to RRF spatial distances ranging from 5 m, 6 m to 7 m across the swimming pool reveal small and comparatively stable distance differences with mean absolute distance differences of 1.8 mm at 5 m, 1.7 mm at 6 m, and 1.5 mm at 7 m. Most pairwise distance differences fall within the range of −3.4 mm to 2.5 mm. This indicates that the adopted air medium refractive index configuration is reasonable in the scenario when both targets of a pair are located in air. Furthermore, can be noted that the ULi systems 3D point clouds in this category are generally the closest to the ground truth given by the IMAGER 3D point clouds.

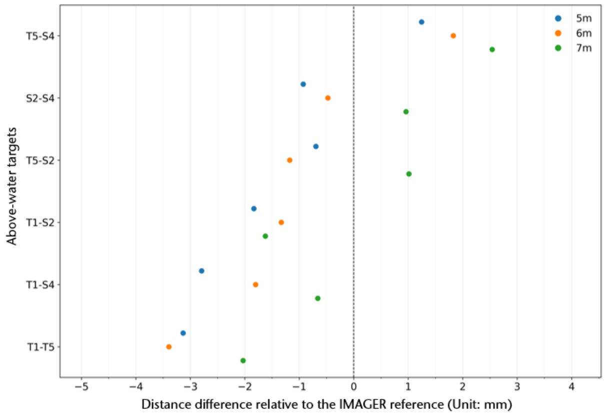

Figure 8 Distance differences of selected above-water targets relative to the mean IMAGER reference. Colors indicate the spatial distances of the ULi system to the RRF across the swimming pool ranging from 5 m, 6 m to 7 m.

3.4.2 RRF structure in cross-medium using targets from both media: To further examine the effect of the cross-medium region of air to water, Figure 9 presents the distance difference of the selected cross-medium target using T-1, T-5, T-7, T-8, S-2, S-4 and S-5 to calculate their distances relative to the mean IMAGER reference for the three spatial distances of the ULi system to the RRF across the swimming pool ranging from 5 m, 6 m to 7 m. The cross-waterline targets show an intermediate but still pronounced discrepancy relative to the IMAGER reference. Compared with the above-water targets, the deviations are substantially larger. The mean absolute distance differences decrease slightly from 12.0 mm at 5 m to 10.9 mm at 6 m and 10.3 mm at 7 m, but the dominant pattern is the same in all 3D point cloud derived distances: the distance differences are mostly negative, meaning that ULi system-derived distances are generally shorter than the IMAGER reference when a target spans the air-water boundary, i.e., waterline. The strongest underestimation is observed for involving target S-5, especially T1-S5, which reaches −32.2 mm to −33.4 mm. This indicates that crossing the waterline introduces a clear systematic bias.

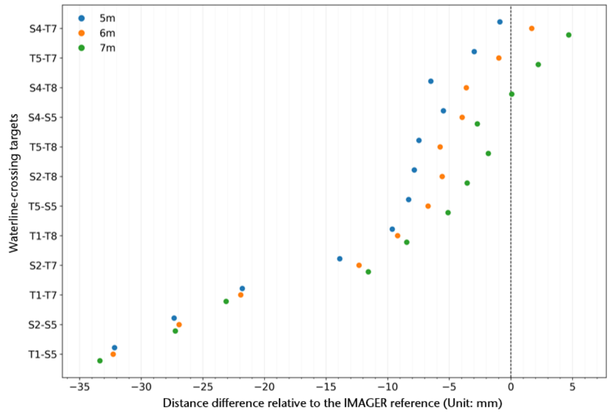

Figure 9 Distance differences of selected cross-medium (waterline) targets relative to the mean IMAGER reference. Colors indicate the spatial distances of the ULi system to the RRF across the swimming pool ranging from 5 m, 6 m to 7 m.

3.4.3 RRF structure in medium water using underwater targets: The analysis of the underwater targets T-7, T-8 and S-5 reveals the internal consistency of the submerged part of the RRF geometry. Figure 10 shows that the underwater targets exhibit the largest difference relative to the IMAGER reference and therefore the weakest alignment with the ground truth. All pairwise distance differences remain negative in all spatial distances of the ULi system to the RRF across the swimming pool ranging from 5 m, 6 m to 7 m, with mean absolute distance differences of 20.2 mm at 5 m, 19.3 mm at 6 m, and 18.6 mm at 7 m. This shows a strong and highly systematic underestimation of ULi system-derived distances once b/w targets and spheres are submerged. Among the selected targets, T8-S5 is the most affected, with distance difference of −27.7 mm to −30.0 mm. The consistent negative pattern for all spatial distances of the ULi system to the RRF suggests that the dominant error source is not random noise but a systematic medium-related modeling effect.

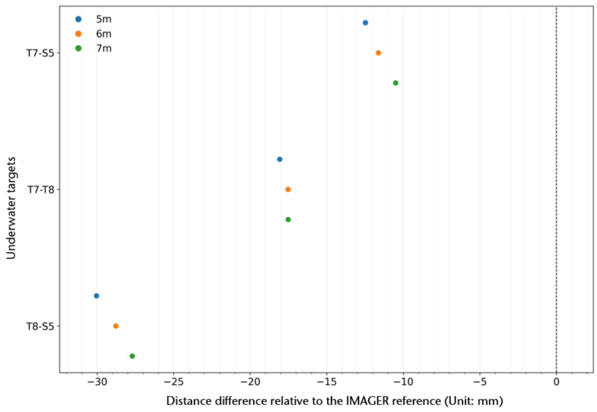

Figure 10 Distance differences of selected underwater targets relative to the mean IMAGER reference. Colors indicate the spatial distances of the ULi system to the RRF across the swimming pool ranging from 5 m, 6 m to 7 m.

4. Conclusions and future work

This study presented a controlled experimental framework based on an RRF structure for evaluating the geometric performance of the ULi system at the particular scenario at the waterline using the IMAGER-derived poolside measurements as the reference. The results showed that the IMAGER-based reference geometry of the RRF remains highly stable throughout the experiment. In addition, the 3D point cloud registration between ULi system and IMAGER achieved millimeter level accuracy for the above-water part. The analysis further demonstrates that applying a single medium configuration for the refractive index to the entire 3D point cloud across different media leads to systematic geometric distortion across the waterline, confirming the necessity of medium-dependent processing. Based on representative rigid-body-invariant pairwise target distances, the results revealed a clear increase in distance difference in cross-waterline and fully submerged targets, indicating that refraction and interface-related effects are the dominant sources of systematic error in cross-medium measurements. Finally, based on the actual temperature, wavelength, and other relevant parameters, a group refractive index of $n_{water,g}$ =1.356 was first derived as the physically justified value, whereas $n_{water,g}$ =1.357 was introduced as an additional sensitivity test. The comparison showed that $n_{water,g}$ =1.356 provided closer results to IMAGER reference than $n_{water,g}$ =1.357 for the underwater and waterline-crossing pairwise target differences. The results demonstrate that the geometric accuracy of the ULi system reconstruction is sensitive to the refractive index setting used in processing.

Future work is dedicated to minimize the geometric errors in the underwater region and at the cross-medium region, i.e., transition from air to water by primarily addressing the group refractive index. In particular, further investigations are needed to determine a proper group refractive index that is appropriate for the specific experiment conditions and sensor configuration. A better understanding and modeling of this parameter will be essential for improving the geometric accuracy of the ULi system-based 3D point clouds across the waterline.

Acknowledgements

We gratefully acknowledge the financial support provided through the Ernst-August Mine Water Monitoring (EAGruMo) project. The project is carried out within the framework of Europa for Niedersachsen, co-financed by the European Union and supported by the Investment and Promotion Bank of Lower Saxony. This funding made an important contribution to the preparation and implementation of the present study and the associated experiments.

We also sincerely thank Fraunhofer IPM for their valuable assistance and technical support throughout the study. Their support was highly beneficial to the successful preparation and execution of the experiments.

References

Fraunhofer IPM, 2025. Inspecting underwater infrastructure. 3D acquisition and monitoring of large underwater structures using LiDAR. ipm.fraunhofer.de (7 January 2026).

Heffner, E., Walter, A. L., Scheider, A., Sternberg, H., 2025. Laboratory-based assessment of the Underwater Laser Scanner ULi. Int. Arch. Photogramm. Remote Sens. Spatial Inf. Sci., XLVIII-2/W10-2025, 123-129. doi.org/10.5194/isprs-archives-XLVIII-2-W10-2025-123-2025

Heffner, E., Semmelroth, C., Sternberg, H., 2026. Untersuchung der Messeigenschaften des Unterwasser-Laserscanners ULi in unterschiedlichen Temperaturbereichen als Grundlage für kombiniertes Unterwassermonitoring. In: Lienhart, W. (ed.), Ingenieurvermessung 2026: Beiträge zum 21. Internationalen Ingenieurvermessungskurs, 10.-13.02.2026 | Graz, Österreich, 108-122. Verlag der Technischen Universität Graz. doi.org/10.3217/978-3-99161-070-0-010

Höhle, J., 1971. Zur Theorie und Praxis der Unterwasser-Photogrammetrie. Schriften der Deutschen Geodätischen Kommission, Series C, No. 163.

Janßen, J., Medic, T., Kuhlmann, H., Holst, C., 2019. Decreasing the uncertainty of the target center estimation at terrestrial laser scanning by choosing the best algorithm and by improving the target design. Remote Sensing, 11(7), 845. doi.org/10.3390/rs11070845

Lan, Y., Yang, J., Kolling, M., Dorndorf, A., Paffenholz, J.-A., 2026. Uncertainty assessment of a green-wavelength LiDAR in laboratory environments. In: Lienhart, W. (ed.), Ingenieurvermessung 2026: Beiträge zum 21. Internationalen Ingenieurvermessungskurs, 10.-13.02.2026 | Graz, Österreich, 95-107. Verlag der Technischen Universität Graz. doi.org/10.3217/978-3-99161-070-0-009

Paffenholz, J.-A., Bae, K. H., 2012. Geo-referencing point clouds with transformational and positional uncertainties. Journal of Applied Geodesy, 6(1), 33-46. doi.org/10.1515/jag-2011-0010

Schwarz, R. K., Pfeifer, N., Pfennigbauer, M., Mandlburger, G., 2020. Depth measurement bias in pulsed airborne laser hydrography induced by chromatic dispersion. IEEE Geoscience and Remote Sensing Letters, 18(8), 1332-1336. doi.org/10.1109/LGRS.2020.3003088

Walter, A. L., Heffner, E., Scheider, A., Sternberg, H., 2025. Underwater laser scanning: Evaluating the performance of ULi in laboratory environments and presenting first insights from real-world applications. The International Hydrographic Review, 31(1), pp. 152-164. doi.org/10.58440/ihr-31-1-n05

Werner, C. S., Gangelhoff, J., Frey, S., Steiger, D., Reiterer, A., 2023. Development of a compact pulsed time-of-flight LiDAR platform for underwater measurements. The International

Hydrographic Review, 29(2), 200–207. doi.org/10.58440/ihr-29-2-n09

Zhang, H., Xu, X., Zhao, H., Dong, F., Qian, Z., Xue, B., 2019. Water temperature and salinity measurement using frequency comb. Applied Sciences, 9(23), 5043. doi.org/10.3390/app9235043

Zhou, S., Guan, Y., Zhan, X., Lu, T., 2008. Robust algorithm for fitting sphere to 3D point clouds in terrestrial laser scanning. Int. Arch. Photogramm. Remote Sens. Spatial Inf. Sci., XXXVII-B5, 519-522.

Zoller + Fröhlich GmbH, 2026. Z+F IMAGER® 5016A, 3D laser scanner. zofre.de/en/laser-scanners/3d-laser-scanner/z-f-imagerr-5016-1 (15 January 2026).